33

Plasma-Driven Flat Panel Displays

Robert T. McGrath
The Pennsylvania State University

Ramanapathy Veerasingam
The Pennsylvania State University

William C. Moffatt
Sandia National Laboratories

Robert B. Campbell
Sandia National Laboratories

33.1 An Introduction to Plasma-Driven Flat Panel Displays

Development History and Present Status

Plasma-driven flat panel display pixels were invented by Bitzer and Slottow at the University of Illinois in 1966 [1-3]. Figure 33.1 shows one of the inventors' early designs and demonstrates its simplicity. Parallel sets of thin conducting wires are deposited on two glass substrates which are then mounted with the conductor sets perpendicular to one another as shown in the Figure 33.1. A spacer, in this case a perforated glass dielectric, is used to maintain a gap separation of about 100 μm between the glass plates. The gap region then is filled with an inert gas, typically at a pressure of half an atmosphere. Individual pixels formed by the intersection of two conductor wires are aligned with the perforations. Pixels are illuminated by applying a voltage between two intersecting wires sufficient to initiate gas breakdown. Over the years, this basic pixel design has undergone a multitude of refinements and improvements, but the fundamental concept is still widely used.

Throughout the 1980s, plasma display products on the market were monochrome and operated with neon-based gases, directly producing within the discharge volume the red-orange (585 to 640 nm) visible photons that are characteristic of the quantum energy level structure of the neon atom. Dot matrix displays of the type shown in Figure 33.2 were widely used [3,4]. Early work by Owens-Illinois led to improvements in glass sealing and spacer supports [5,6], and work by IBM led to improved understanding

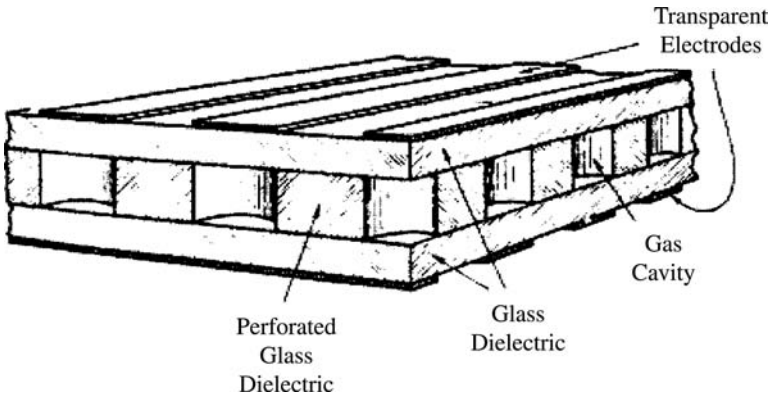

FIGURE 33.1 Structure of the ac plasma display invented at the University of Illinois. (From Bitzer, D.L. and Slottow, H.G., *AFIPS Conf. Proc.*, Vol. 29, p. 541, 1966. With permission.)

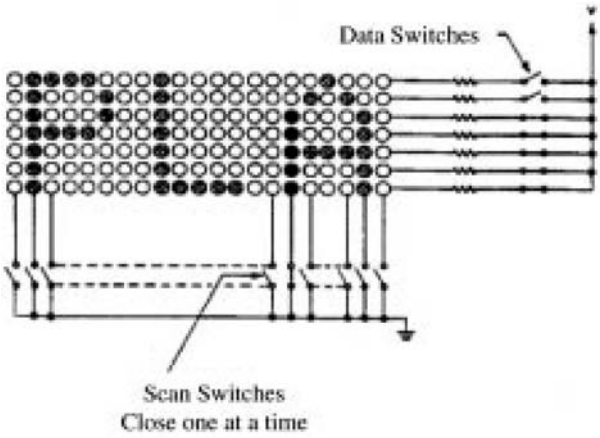

FIGURE 33.2 A simple dot matrix plasma display and data scanning switches. (From Weber, L.F., in *Flat Panel Displays and CRTs*, L.E. Tannas, Jr., Ed., Van Nostrand Reinhold, New York, 1985. With permission.)

and control of the discharge [7-15]. These advances ultimately paved the way for manufacture of large-area, high-resolution monochrome displays. The largest area plasma display panels ever manufactured were produced by Photonics Imaging. These monochrome displays had a 1 m diagonal dimension and contained over 2 million pixels with a pixel pitch of 20 pixels/cm (50 lines/in.) [4].

Advances in lithography, patterning, and phosphors have enabled continued improvement of plasma display performance and resolution. Today, many companies offer full-color plasma flat panel displays. Table 33.1 presents a summary list compiled by the National Research Institute of display panel specifications for some of the major companies investing in plasma flat panel manufacturing [16]. According to Stanford Research, Inc., sales for plasma display panels in 1995 totaled $230 million, but projected sales for 2002 are $4.1 billion [17]. NEC projects a more aggressive market growth reaching $2.0 billion by the year 2000 and $7.0 billion by 2002 [17]. The production capacities listed in Table 33.1 represent investments committed to manufacturing as of January 1997. As these production facilities come online, color plasma flat panel display production will grow to nearly 40,000 units per month by the end of 1998, and to over 100,000 units per month by early in 2000. In 1993 Fujitsu was the first to market a high-information-content full-color plasma flat panel display, a 21 in. diagonal, ac-driven system with a 640 × 480 pixel array [17,18]. Two examples of more recent market entries are shown in Figures 33.3 and 33.4. The first example is the NHK full-color, 102 cm (40 in.) diagonal, high-definition television

TABLE 33.1 Plasma Flat Panel Display Specifications and Manufacturer's Business Plans

	Product Specification			Efficiency Specification				Plan			
Company	Inch	Aspect	Pixels	Luminecence (cd/m^2)	Contrast	lm/W	Power (W)	Factory	Capital Cost ($M)	Product Ability unit/month	Target Region
Fujitsu	42	16:9	852 × 480	300	70:1	0.7	350(set) 300(panel)	Miyazaki	20	10,000	Europe (Philips), Japan
NEC	33	4:3	640 × 480	200	150:1	1.2	270(set) 190(panel)	Tamagawa, Kagoshima	5	2,000	Japan
Pioneer	40	4:3	640 × 480	400	150:1	1.2	350(set)	Kofu	5	10,000	Japan
Mitsubishi	40	4:3	640 × 480	350	200:1	0.8	350(set) 300(panel)	Kyoto	14.8	10,000	U.S.
MEC	42	16:9	852 × 480	450	150:1	10	300(panel)	Kyoto	10	5,000	Japan, U.S.
Photonics	21	5:4	1280 × 1024	100	50:1	—	300(panel)	Ohio	—	—	—
Hitachi	25	4:3	1024 × 768	150	50:1	—	250(set)	Yokohama	3	1,000	—
NHK	40	16:9	1344 × 800	93	80:1	—	—	—	—	—	—

Source: Wakabayshi, H., paper presented at *Imaging 2001: The U.S. Display Consortium Business Conference,* January 28, San Jose, CA, 1997. With permission.

FIGURE 33.3 The 40-in. diagonal dc-driven plasma display from NHK. (From Mikoshiba, S., *Inf. Display,* 10(10), 21, 1994. With permission.)

(HDTV) [19-22]. The system comprises 1,075,000 full-color pixels (1344 × 800) with a pixel pitch of 0.65 mm in both horizontal and vertical directions (15.4 pixels/cm). This pulsed, dc-driven display has a peak luminance of 93 cd/m^2, a contrast ratio of 80 to 1, and produces 256 gray levels. The display has an overall thickness of only 8 cm and weighs only 8 kg. The dimensions of the display panel itself are 87.5 × 52.0 cm with a width of only 6 mm. Shown in Figure 33.4 is the 76 cm (30 in.) diagonal, full-color ac Plasma Display manufactured by Photonics Imaging [23-24]. The display contains an array of 1024 × 768 full-color pixels. At 16.8 pixels/cm (pixel pitch = 0.59 mm) this is the highest resolution full-color, plasma display manufactured to date. This unit has 64 gray levels per color channel and an average area (white) luminance greater than 103 cd/m^2 (30 fL).

Dc and Ac Plasma Pixels

As indicated above, plasma display pixels can be designed for either ac or dc operation. Figure 33.5 shows schematic diagrams for the simplest dc and ac pixel designs. In either case, sets of parallel conductor wires are deposited on glass substrates. In most cases display costs are kept low by utilizing ordinary soda-lime float glass. The two glass plates are then mounted with a separation of about 100 μm and with the conductor wire sets perpendicular to one another. The gap region between the glass plates is filled with an inert gas, which discharges and illuminates the pixels when sufficient voltage is applied across two intersecting wires.

For dc pixels, shown in Figure 33.5a, the working gas is in direct contact with the electrodes. Electrons produced within the discharge volume flow rapidly to the anode, while ions produced flow more slowly toward the cathode. At 53.3 kPa (400 torr), a gas gap of 100 μm, and an applied voltage of 200 V, the electron and ion transit times across the gap are roughly 0.2 and 20 ns, respectively. Once breakdown is initiated, the electrical resistance of the discharge is negligible. Consequently, dc operation requires that external resistors in series with each pixel be included in the circuit in order to limit the current amplitude. Often, dc pixels are operated in pulsed discharge mode with frequency modulation used to define the pixel brightness. For either ac or dc pixels, a base firing frequency of 50 kHz is typical. This frequency is too fast for the human eye to detect any *on–off* flicker, but allows sufficient flexibility for intensity and refresh control. In reviewing the literature on plasma displays, it is easy to confuse dc and ac pixels since dc pixels are often operated in pulsed mode and with electrode polarity reversal which distributes sputter damage over both electrode surfaces. The dc pixels are readily identified by conducting electrodes in direct contact with the discharge gas and the inclusion of a current-limiting resistor in the circuit for each pixel. While polarity reversal is optional for dc pixel operation, it is inherently required for ac pixel

FIGURE 33.4 The 40-in. diagonal ac-driven plasma display from Photonics Imaging. (From Friedman, P.S., *Inf. Display,* 11(10), October 1995. With permission.)

operation as discussed below. Drive electronics, current limiting, gray scale, and other aspects of both dc and ac pixel operation are discussed in greater detail in subsequent sections.

Figure 33.5b shows a schematic representation of an ac plasma pixel configuration. One can see that the differences between ac and dc pixel geometry are slight; however, the resulting operational differences are significant. In the ac pixel, the conductor wires are covered with a dielectric film. Typically, lead oxide (PbO), which has a dielectric constant of about 15, is deposited at a film thickness of about 25 μm. Most ac pixels are made with a thin film (50 to 200 nm) of magnesium oxide (MgO) dielectric coating covering the PbO and in contact with the working gas. This dual material dielectric film serves two principal functions, charge storage and secondary electron emission.

The exact voltage required for gas breakdown depends upon the gap width, the gas pressure, the gas composition, and MgO surface conditioning. For the pixel parameters shown in Figure 33.5b, an externally applied voltage of about 120 to 180 V is required to initiate a discharge. In the ac pixel, once the discharge is initiated, electrons and ions flow toward the anode and cathode, respectively, as in the dc pixel. However, in the ac case, charge carriers are unable to reach the conductor wires and instead collect as a surface charge on the dielectric coating. The electric field within the gas gap is always the sum of that produced by the externally applied voltage and that produced by the surface charge. During pixel firing, if the externally applied voltage is held constant for only a few microseconds, the net electric field within the gas gap very quickly decreases (~100 to 200 ns). The gap potential drop produced by the surface charge shields out that produced by the externally applied voltage. Eventually, the gap electric field is insufficient to sustain the discharge and the pixel turns *off*. Thus, each ac pixel is inherently

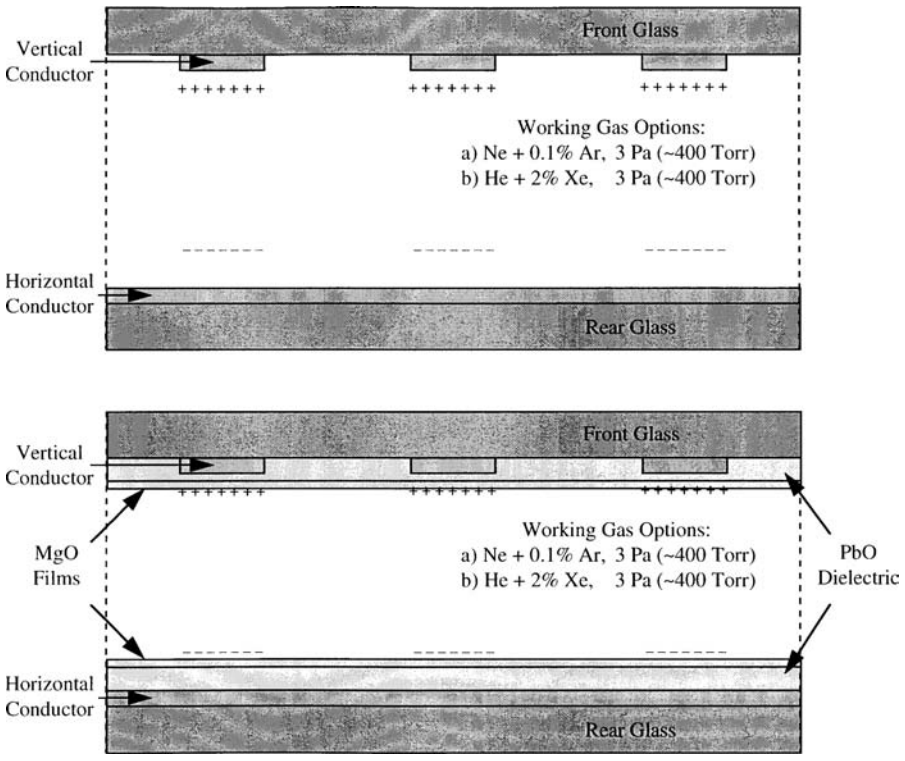

FIGURE 33.5 Schematic diagrams of (a) dc and (b) ac opposed electrode plasma pixels.

self-current-limiting and, unlike the dc pixel, requires no external resistance in series with it. At the start of the next ac half cycle, the externally applied voltage is reversed. When this occurs, the voltage across the gas gap is the sum of the external voltage and the voltage produced by the surface charge established during the previous discharge. If a sufficient surface charge is present, a new discharge pulse can be initiated by application of an external voltage, which by itself would be insufficient to break down the gas. Within the new discharge, charge carriers flow quickly to reverse the polarity of the surface charge concentrations. Once again, the field within the gap is diminished and the discharge turns *off*. Storage of surface charge make ac pixels easily controllable and provides them with their inherent memory properties. The presence or absence of surface charge determines whether or not a given pixel will discharge at the onset of the next ac half cycle of the externally applied voltage. The details of how these discharge dynamics are used to write, erase, and sustain each pixel are discussed in subsequent sections, along with drive mechanisms for gray scale and for pixel array refresh.

General Attributes of Plasma Displays

Plasma-driven flat panel displays offer a number of advantages over competing display technologies. The highly nonlinear electrical behavior of each pixel, with inherent memory properties, can be used to advantage in design of the drive electronics required to refresh and to update the pixel array of the display. The simplicity of the pixel design makes large-area manufacturing problems, such as alignment and film thickness uniformity, somewhat more manageable. Relative to color active matrix liquid crystal displays (AMLCDs) which use a thin-film transistor (TFT) to control each pixel, less complicated manufacturing and less complicated drive electronics give plasma flat panel displays advantage for large-area applications. On the other hand, plasma displays require more robust drive electronics with voltages of 100 to 275 V. Plasma displays are also not well suited for portable applications since power consumption is high relative to other display technologies, but not restrictive for office or domestic use. The 76 cm (30 in.) diagonal

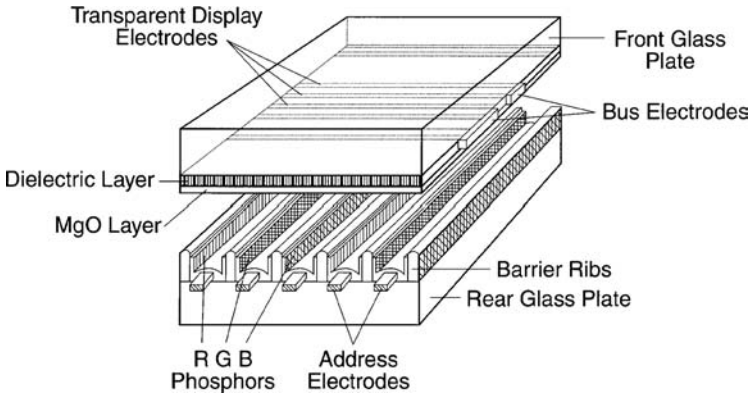

FIGURE 33.6 Structure of the ac color plasma display manufactured by Fujitsu. (From Mikoshiba, S., *Inf. Display,* 10(10), 21, 1994. With permission.)

color display manufactured by Photonics Imaging shown in Figure 33.4 has a peak power consumption of only 300 W [23]. At high power levels, plasma-driven flat panel displays are bright enough to be readable in sunlight. The displays are also easily adjusted to a low-ambient-light condition by discharge amplitude or frequency modulation.

Plasma flat panel displays are well suited for large-area (0.5 to 5 m) applications such as videoconferencing, large meeting room displays, outdoor displays, and simulators requiring large viewing areas. Thin, high-resolution, large-area, color plasma displays are also very attractive for desktop workstation or personal computer applications requiring high-resolution graphics. Note, too, that plasma flat panel displays have very large viewing angles, greater than 160° in many designs [22-24]. For displays using metal electrodes, one often finds that the best viewing angle is slightly off normal since the front electrode wire blocks out a portion of the pixel emission. This occurs both for monochrome pixels producing visible emissions within the discharge and for color plasma displays where the viewer sees visible red, green, and blue (RGB) emissions from vacuum ultraviolet (VUV) photon-stimulated phosphors. Some manufacturers have investigated use of transparent electrodes, such as indium-tin oxide (ITO), but there is a trade-off with power consumption since the conductivity of ITO is less than that of metal electrodes [18]. In contemporary designs, the metal conductor width is thin (~20 μm) and its opacity does not present a major problem.

For color pixels, the discharge gas mixture is modified to produce emissions in the VUV. In all other respects, the operational principals of the plasma discharge by the pixel are identical for color and for monochrome displays. Ideally in color plasma displays, no visible emissions are produced within the discharge itself and VUV-photostimulated luminous phosphors are used to produce the required RGB visible light. The ac color pixel design concept shown in Figure 33.6 is that utilized by Fujitsu [18]. Long, straight barrier structures, each about 100 μm tall, are constructed parallel to and between each of the vertically oriented conductor wires on the rear glass plate. The sidewalls of these barriers are alternately coated with red, green, and blue photostimulated phosphors. Note that the Fujitsu panel employs a three-electrode, ac-driven surface discharge pixel design which is slightly more complicated than the opposed electrode ac design shown in Figure 33.5b. This chapter will return to surface discharge configurations and other aspects of color pixel design and operation after reviewing fundamentals of the discharge physics and electrical behavior governing pixel operation.

33.2 Fundamentals of Plasma Pixel Operation

Atomic Physics Processes

Although simplistic in design, the plasma display pixel is a rich environment for study of basic atomic physics, electron collisional processes, photon production and transport, and plasma–surface interactions.

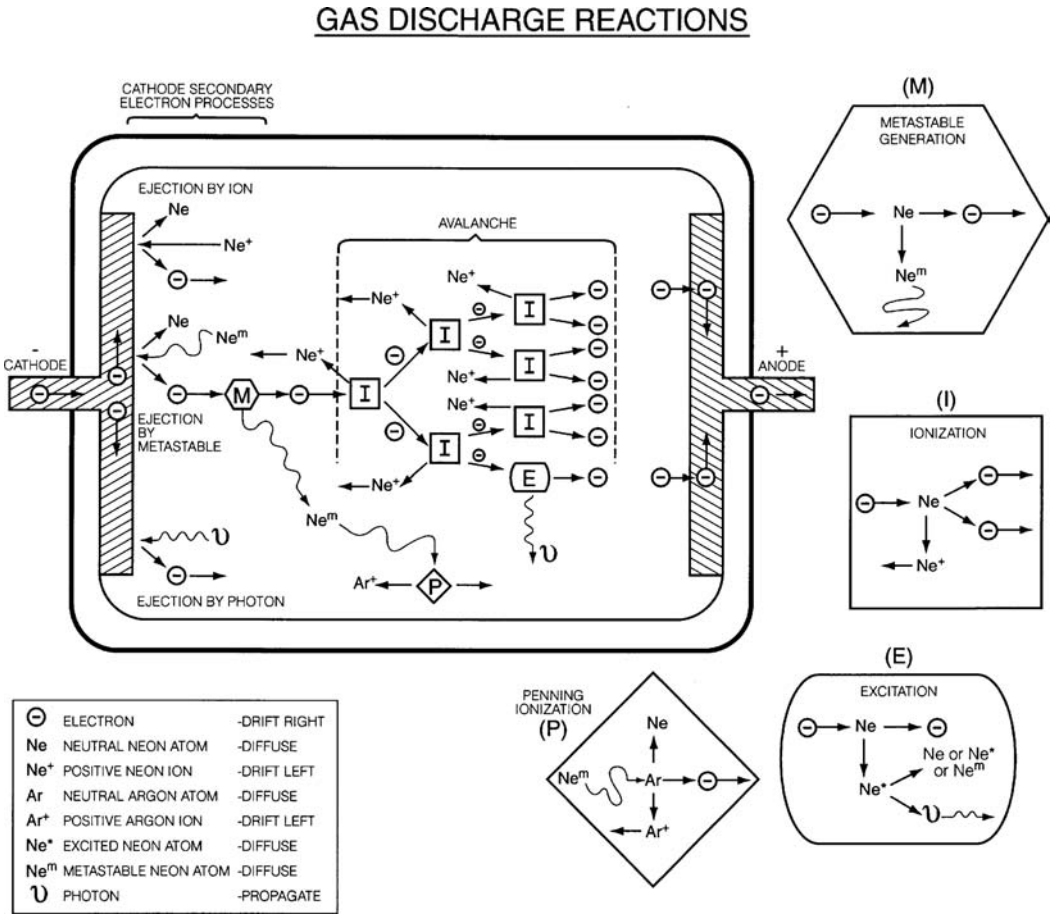

FIGURE 33.7 Collisional and surface interactions in a gas discharge. (From Weber, L.F., in *Flat Panel Displays and CRTs,* L.E. Tannas, Jr., Ed., Van Nostrand Reinhold, New York, 1985. With permission.)

The coupling of these processes for a neon–argon monochrome pixel discharge was nicely summarized in the diagram from Weber which is reproduced here as Figure 33.7 [4]. The reader interested in additional information on fundamental discharge physics is directed to one of the excellent textbooks in this field [25–27].

The physical processes governing the behavior of the pixel discharge are closely coupled and form a closed-loop system. The discussion begins by assuming that a seed electron is resident within the gas gap and is subjected to an electric field which results from application of an externally applied voltage to the two conductors forming that pixel. Some of the gas and surface processes for production of the seed electrons will become evident as the discussion progresses. In order to ensure reliable discharge initiation, seed particles, which are either electrons or electron-producing photons or metastable atoms, are often provided by a controlled source which may be external to the pixel being fired. Some display panels include electrodes for production of seed particles at the edges of the panel outside the field of view or hidden behind opaque conductor wires. Other display panels use well-controlled temporal sequencing to ensure that nearest-neighbor pixels provide seed particles for one another [4,19,28]. Pixel addressing sequences are discussed further later in this chapter.

The transport of electrons or ions across the gas gap is a balance between field acceleration and collisional energy loss. In the example of Figure 33.7, the gas is mostly neon (98 to 99.9%) and field-accelerated electrons will predominantly collide with Ne atoms. The quantum energy level diagram for

excitation of the Ne atom is shown schematically in Figure 33.7 [29]. Note that the lowest-lying excited state is 16.6 eV above the ground state, while the ionization energy is 21.6 eV. This means that electrons with energies less than 16.6 eV can only experience elastic collisions with the Ne atoms. When an electron is field-accelerated to an energy in excess of 16.6 eV, inelastic collisions which transfer energy from the incident electron to one of the outer-shell electrons in the Ne atom can take place. Incident electrons with kinetic energies in excess of 21.6 eV can drive ionization reactions:

$$\mathrm{Ne} + \mathrm{e}^- \rightarrow \mathrm{Ne}^+ + 2\mathrm{e}^- \tag{33.1}$$

Excitation and ionization collisions transfer energy from the electron population to the neutral atoms in the gas. At the same time, the electron population available to ionize the Ne further is increased with every ionizing event. The result is the discharge avalanche schematically shown in Figure 33.7, which manifests itself experimentally as a rapid increase in electric current flowing in the pixel gas gap. In dc panels, an external resistor of about $R = 500\ \mathrm{k}\Omega$ is placed in series with each pixel. The amplitude of the externally applied voltage provided by the driving electronics, V_a, is held constant and the total voltage across the gas gap, $V_g = V_a - IR$, decreases as the circuit current, I, increases. Very quickly, a steady-state dc current in the gas gap and in the circuit is established. Brightness and gray scale are controlled by frequency modulation of the pulsed dc pixel firing using a base frequency of about 50 kHz. In ac pixel discharges, electrons and ions are driven by the applied field to the dielectric-covered anode and cathode, respectively. The buildup of charge on the dielectric surfaces shields the gap region from the field produced by the externally applied voltage. Eventually, the electric field in the gap drops below a level sufficient to sustain the discharge and the pixel turns *off*.

For electron energies greater than 16.6 eV, collisions with Ne atoms can excite outer-shell electrons in the atom to one of the numerous excited energy states shown in Figure 33.7.

$$\mathrm{Ne} + \mathrm{e}^- \rightarrow \mathrm{Ne}^{\mathrm{ex}} + \mathrm{e}^- \tag{33.2a}$$

$$\mathrm{Ne}^{\mathrm{ex}} \rightarrow \mathrm{Ne}^* + h\nu \tag{33.2b}$$

Most of these excited states have short lifetimes ranging from fractions to tens of nanoseconds [30] and quickly decay to lower-lying atomic quantum states accompanied by the emission of a characteristic photon, indicated in Equation 33.2 by $h\nu$, the product of Planck's constant times the photon frequency. As can be seen in Figure 33.8, the characteristic red-orange Ne gas emissions result from electron transitions within the atom from higher-energy 2p quantum states to lower-lying 1s energy levels [30,31]. Two of the four 1s energy levels radiate to ground-emitting VUV photons with wavelengths of 74.4 and 73.6 nm. Due to quantum mechanical exclusion principles, electron decay from the other two 1s levels is more complex and depends upon fine details of the electronic wave function and upon very small perturbing interactions [31]. Consequently, decay lifetimes for these so-called metastable states are measured in seconds, which is very long relative to other dynamic physical processes governing pixel discharge behavior, such as charge or neutral particle transport. An Ne atom with an electron trapped in one of these metastable levels harbors 16.6 eV of latent energy. The metastable atom, Ne*, is unable to dissipate its stored energy in collisions with ground-state Ne atoms, yet readily liberates its energy whenever a lower-lying energy configuration can be accessed. The principal channels in this system to lower energy configurations are Ne* collisions with Ar or Ne* incidence onto pixel interior surfaces.

Figure 33.8 shows simplified energy-level diagrams for several inert gases. The relative positioning of the allowable energy levels provides insight into the energy exchange that occurs in collisional coupling. The ionization energy of the Ar atom is 15.8 eV and lies 0.8 eV below the metastable-state Ne*. Consequently, the Ne* has sufficient stored energy to ionize the Ar atom:

$$\mathrm{Ne}^* + \mathrm{Ar} \rightarrow \mathrm{Ne} + \mathrm{Ar}^+ + \mathrm{e}^- \tag{33.3}$$

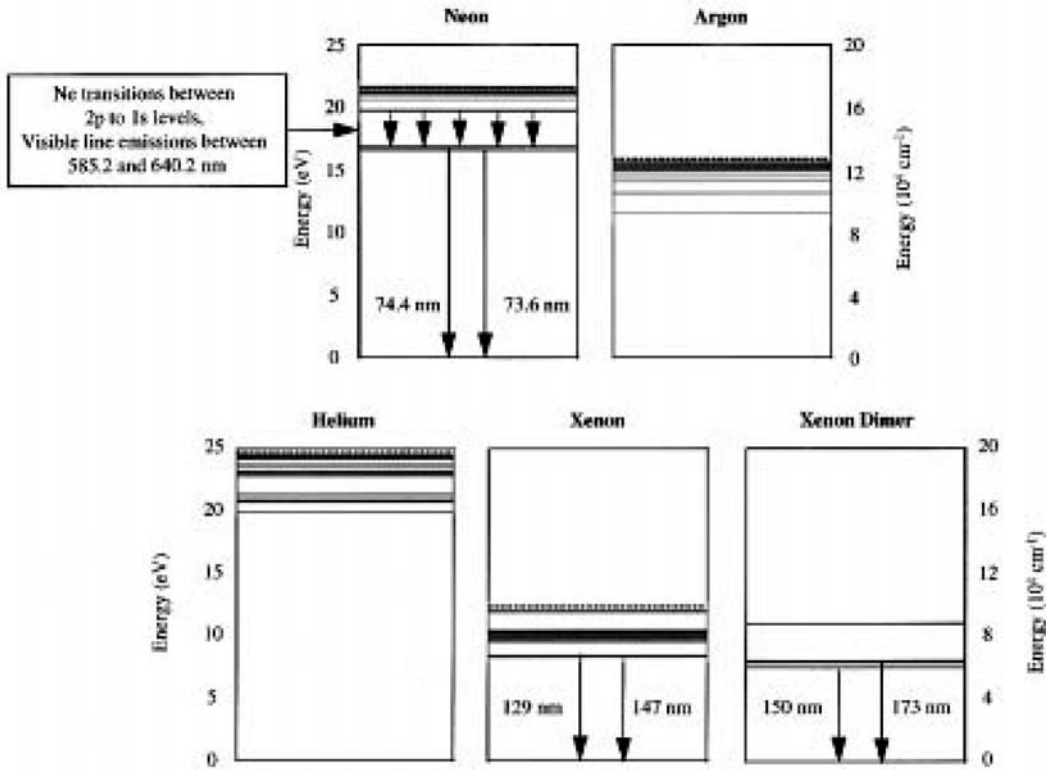

FIGURE 33.8 Quantum energy level diagrams for He, Ne, Ar, Xe, and the Xe^{2*} dimer.

Ionizing reactions of this type are called Penning reactions, and gas mixtures that rely on metastable states of the majority gas constituent (Ne) for ionization of the minority gas constituent (Ar) are referred to as Penning gas mixtures [25,26,32]. Figure 33.9 shows the efficiency with which charge pairs are produced through ionization within Ne/Ar Penning gases containing various fractions of Ar. The curves show that for any given pressure, ion pair production per volt applied is optimal at low Ar gas fractions (0 to 10%) except for very large values of E/P, greater than 75 V/m/Pa (100 V/cm/torr), where E is the electric field strength and P is the gas pressure. Penning gas mixtures have been studied for many years. Figure 33.9 shows the original data on Ne/Ar gas breakdown published by Kruithof and Penning in 1937 [32]. An extensive volume of literature has been published on inert gas Penning processes since then, and the interested reader is referred to the excellent texts which have recently been re-released through the American Vacuum Society and MIT Press [25,26].

Plasma display pixels usually operate at pressures near 53.3 kPa (400 torr) in order to achieve sufficient photon production and brightness. Typical pixel fields are roughly 100 MV/m. Consequently, plasma pixels operate with E/P values near 18.8 V/m/Pa (25 V/cm/torr). Both charge pair production and luminous efficiency are then optimized with Ar gas fractions between 0.1 and 10%, depending upon the specifics of the pixel gas pressure, gap width, and driving voltage. For a given applied voltage, the product of the gas pressure (P) and the gas gap dimension (d) provides a measure of the balance between electron acceleration by the electric field and electron energy loss due to collisions with the background gas. Paschen curves, which plot the gas breakdown voltage vs. the Pd product, for several inert gas mixtures are shown in Figure 33.10 [26,33,45]. In each case, minimum voltage for breakdown occurs at a value of the Pd product which is dependent upon the ionization levels, collisionality, and energy channels within the gas. For example, in Ne atomic excitation and ionization processes dominate, while in air much of the energy absorbed by the gas goes into nonionizing molecular vibration, rotation, and dissociation. For fixed pressure, the Paschen curves show that increased gap dimension lowers the electric

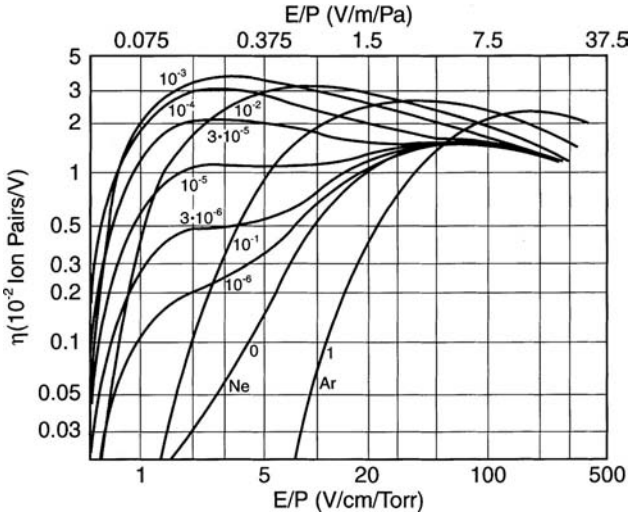

FIGURE 33.9 Ionizing collisions plotted vs. electric field strength divided by pressure. The numbers on each curve indicate the ratio of the Ar partial pressure to the total gas pressure. (From Brown, S., *Basic Data of Plasma Physics — The Fundamental Data on Electrical Discharges in Gas,* American Institute of Physics Press, New York, 1993. With permission.)

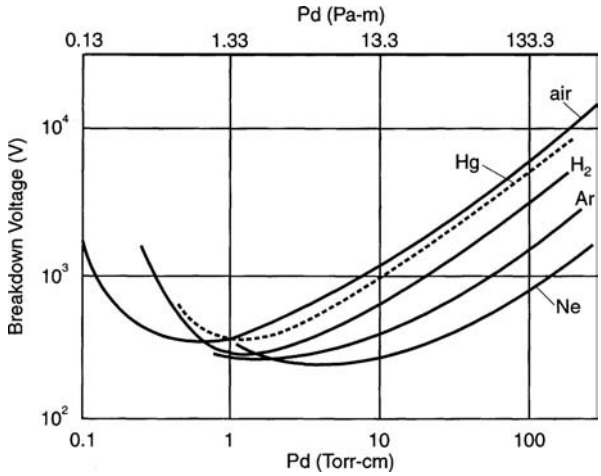

FIGURE 33.10 Breakdown voltage as a function of pressure — gas gap length product for various gases. (From Brown, S., *Basic Data of Plasma Physics — The Fundamental Data on Electrical Discharges in Gas,* American Institute of Physics Press, New York, 1993. With permission.)

field strength per volt applied and a large voltage is required for breakdown. On the other hand, if *d* is reduced for a given pressure, the electric field strength can be large, but electrons transit the gap without initiating a sufficient number of collisions to drive the type of discharge avalanche shown in Figure 33.7. If the gas gap, *d,* is held fixed while pressure is varied, the shapes of the Paschen curves are again explained by electron acceleration and collisional processes. For high pressures, the mean free paths between electron collisions with the background gas atoms are short and electrons are unable to accelerate to energies sufficient to initiate ionization unless the electric field is especially strong. At low pressures, the electrons may be accelerated by the field to energies sufficient to initiate ionization, but few collisions with the background gas occur and, again, the avalanche is difficult to initiate. Penning processes are especially efficient at driving ionization. Introduction of 0.1% Ar into the neon gas lowers the minimum breakdown

voltage from the value near 250 V shown in Figure 33.10, to about 150 V. The minimum breakdown voltage occurs at a *Pd* product of 40 Pa·m (30 torr·cm) for this gas mixture.

Discharge Physics for Plasma Pixels

Within any discharge, electrons move very quickly, while the more massive ions move relatively slowly in comparison. In a charge-neutral plasma that is subjected to an externally applied electric field, the mobile electrons quickly respond to the applied field and rush toward the anode. The inertia-laden ions, in a much slower fashion, begin their motion toward the cathode. Very quickly, a local charge imbalance is established as the electrons reach the anode faster than the rate of arrival of ions at the cathode. Poisson's equation

$$\nabla \cdot E(x) = 4\pi\rho(x) = 4\pi e\left(n_i(x) - n_e(x)\right) \tag{33.4}$$

shows that a local electric field is established in response to the net positive charge density, $\rho(x)$, in the plasma region. Here, $n_i(x)$ and $n_e(x)$ are the spatial profiles of the ion and electron densities, respectively, and e is the electron charge. The field established retards the rate at which electrons flow out of any volume within the plasma column and forces them to follow the net ion motion. The ion drift motion is correspondingly accelerated, but this acceleration is smaller by a factor proportional to the mass ratio of the electron to the ion. The net ion/electron motion is called ambipolar flow and is described in detail in many basic plasma physics texts [25-27].

In steady-state dc plasma pixel discharges, the amplitude of the current flowing in the circuit and in the gas gap is defined by the value of the applied voltage and the resistor in series with the pixel. Steady-state operation dictates that charge buildup within the gap region cannot occur. The rate at which charge particle pairs arrive at the electrodes must equal their rate of production due to ionization. At the same time, the rates at which ions and electrons leave the plasma volume, arriving at the cathode and anode, respectively, must be equal. Equilibrium is sustained by establishment of the spatial potential profile within the gas gap shown in Figure 33.11a. Due to the high electron mobility, the plasma is extremely efficient in shielding out externally applied electric fields. As a result, the potential profile is flat across the gas gap of a pixel sustaining a fully developed discharge. The entire potential drop is localized in a small zone called the sheath adjacent to each electrode. The spatial extent of the sheath is determined by the effectiveness of the electron population in shielding out the electric fields produced by the electrode potentials. The Debye length,

$$\lambda_D = \sqrt{kT_e / 4\pi e^2 n_e(x)} \tag{33.5}$$

provides a measure of the shielding distance. The expression for λ_D implies that the sheath thickness increases with increasing electron temperature, T_e, and decreases as the electron density, n_e, increases. For fully developed plasma pixel discharges, the product of Boltzmann's constant and the electron temperature, kT_e, is at most a few electron volts, and n_e is of order $10^{16}/m^3$. Thus, the sheath thickness is roughly 5 μm. The potential within the plasma region adjusts, V_P, within the discharge volume rises to a value just above that of the applied voltage at the anode. Consequently, only the most energetic electrons can overcome the potential barrier at the anode which adjusts to a potential such that the rate of electron loss at the anode equals the rate of ion loss at the cathode. For ac plasma pixels, a similar potential profile is established, but changes dynamically as the pixel pulse evolves. Charge pairs incident upon the anode and cathode in ac pixels are trapped there by the dielectric film covering the conductor wires. Consequently, the potential at the discharge boundary is diminished as surface charge collects at each electrode, as shown in Figure 33.11b. Ultimately, the discharge terminates as the electric field produced by the surface charge cancels that produced by the externally applied voltage. As the density of charge carriers is reduced near the termination of an ac pixel discharge pulse, the effectiveness of the

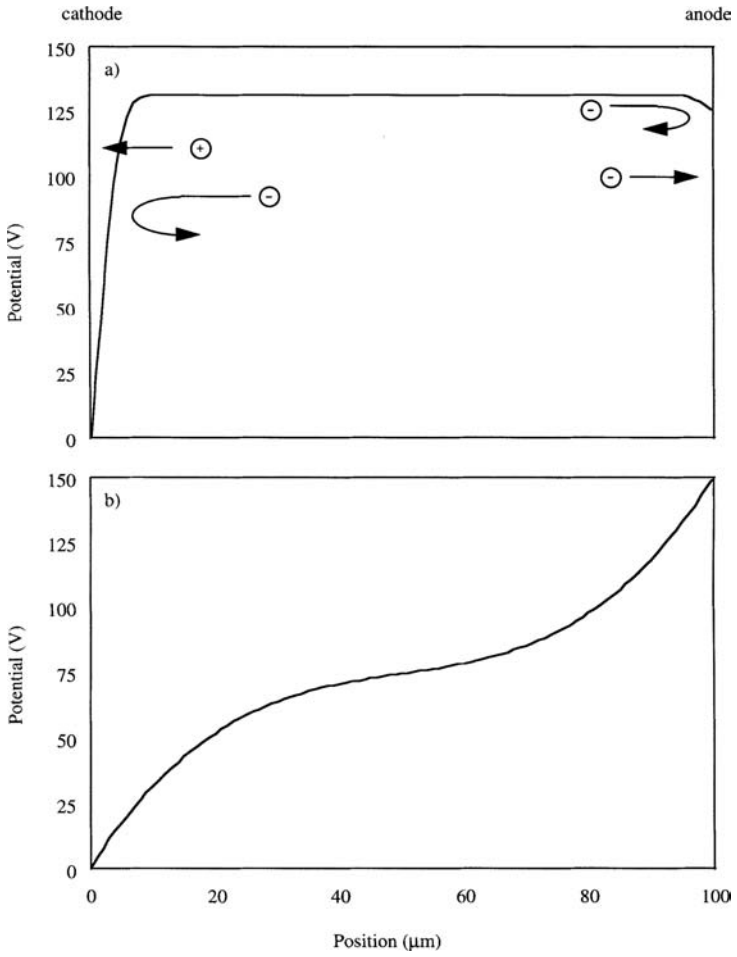

FIGURE 33.11 Potential profiles in the pixel gap region for (a) high-electron-density and (b) low-electron-density discharges.

electrons to shield out electric fields within the gap is diminished. In this situation, the sheath potential drop is small but the sheath region occupies a large fraction of the gap [36,37].

Plasma Surface Interactions

Ion-Induced Secondary Electron Emission

Ions arriving at the cathode sheath are accelerated by the sheath potential drop. Incident ions strike the cathode with kinetic energies equal to the plasma potential, V_p, which is just over 200 V in the example shown in Figure 33.12a. Ions incident on the cathode quickly capture an electron, additionally depositing on the cathode surface an energy equal to the recombination or ionization energy for that atom. Energy deposition on the cathode surface drives two important processes for plasma pixels — ion-induced secondary electron emission and sputtering. The first process significantly enhances the luminous efficiency of plasma pixels. The second shortens their operational lifetime as is discussed in subsequent sections.

Ion-induced secondary electron emission occurs when ion energy deposition on the surface results in electron ejection. Secondary electrons are exceptionally effective at driving discharge ionization since they gain large amounts of kinetic energy as they are accelerated across the cathode sheath and because

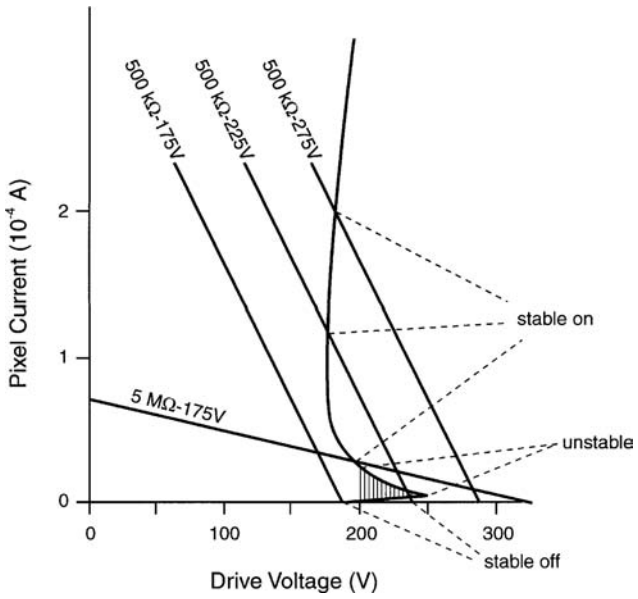

FIGURE 33.12 A representative current–voltage characteristic for gas breakdown. Load lines representative of plasma pixel operation are also shown. (From Weber, L. F., in *Flat Panel Displays and CRTs*, Tannas, L. E. Jr., Ed., Van Nostrand Reinhold, New York, 1985. With permission.)

they have ample opportunities for ionizing collisions as they traverse the entire width of the gas gap. The secondary electron emission coefficient, γ, is defined as the number of electrons ejected per incident ion [25,26]. As one would expect, γ varies with incident ion energy and with cathode material. Most ac plasma display panels take advantage of the strong secondary electron emission of MgO, which is also a good insulating material as required for surface charge storage in ac operation. Measurement of the MgO γ value is difficult, especially for low-energy ion incidence (<500 eV), and is complicated by charge buildup on the samples during the measurements [38]. Most often, relative values of secondary electron yields for different materials are deduced from discharge intensity measurements [11,12,39-42]. Chou directly measured the ion-induced secondary electron emission coefficient for MgO using a pulsed ion beam with sample surface neutralization between pulses. For ion incidence at 200 eV, he found $\gamma = 0.45$ and $\gamma = 0.05$ for Ne^+ and Ar^+, respectively [39]. Note, too, that photons and metastable atoms incident on the electrode surfaces are also capable of initiating secondary electron emission, as shown in Figure 33.7. Since neither photons nor metastables are influenced by the electric fields within the gas gap, they propagate isotropically throughout the gas volume and are often utilized as seed particles.

Sputtering

Ions accelerated across the sheath deposit energy on the cathode surface. This often initiates sputtering, whereby an atom within the cathode material is ejected from the surface. Sputtering processes erode the cathode surface and degrade pixel performance. Contamination of the discharge by sputtered surface impurities can lead to reduction in luminous efficiency due to visible emissions from the contaminant atoms or molecules which compromise the color purity of the pixel. Unwanted surface coatings from redeposited materials can also degrade the electrical characteristics of the pixel or, in color applications, shield the phosphors from VUV photons, further degrading luminous efficiency. For argon ion, Ar^+, bombardment of MgO surfaces at 2 keV, the measured sputtering yield is slightly greater than one ejected atom per incident ion [43]. Data on sputtering yields at lower energy ion incidence are difficult to obtain. Because yields are small, large incident ion currents are required to obtain measurable signals and sample charging is once again a problem. In spite of the lack of detailed data on low-energy MgO sputtering, manufacturers of ac plasma panels have been able to demonstrate display lifetimes well in excess of

10,000 h [18,23]. Shone et al. [44] have demonstrated that Rutherford backscattering of high-energy (2.8 MeV) alpha particle can be used to measure the thickness of MgO film on a PbO substrate. The film thickness accuracy obtained was ±1.5 nm. Because the technique requires a large (and expensive) particle accelerator, this technique is a very nice research tool but is ill suited for any fabrication line measurements.

33.3 Pixel Electrical Properties

Electrical Properties of Dc Pixels

Figure 33.5 shows schematic diagrams and circuit models for dc and ac pixels. In the dc case, the pixel gas gap functions electrically as a variable impedance resistor. Prior to gas breakdown, the resistance is large and the pixel represents an open-circuit element. Once breakdown is initiated, the plasma is an excellent conductor and offers only modest resistance, R_P, to current flow. Since $R \gg R_P$, the circuit equation simplifies to

$$V_a = I\left(R + R_p\right) \approx IR \tag{33.6}$$

and the circuit current, I, is defined by the amplitude of the applied voltage and the size of the circuit series resistor, R. The externally applied voltage, V_a, is typically a 50 kHz square wave with a fast voltage rise time (~50 ns). The dc driving voltages range from 175 to 275 V and a typical value for the series resistor is $R = 500$ kΩ. Pixel currents then range from 0.35 to 0.55 mA. Note that without a large resistance in series with the pixel, the current is limited by some physical failure such as melting of the pixel electrodes.

Figure 33.12 shows the characteristic *I–V* behavior of a dc pixel which has a breakdown voltage of 250 V [4]. Only a very small current due to a few stray charge carriers flows across the gas gap as the voltage increases from 0 to 250 V and the pixel remains in the *off* state. At the breakdown voltage, the situation is dynamic with the current growing rapidly and the voltage across the gas gap dropping as a result. The steady-state operating point achieved is identified by the intersection of the load line, $V_a = IR$, with the discharge *I–V* characteristic as shown in Figure 33.12. For an applied voltage of 175 V the pixel is always *off*, while for $V_a = 275$ V the pixel is always *on*. For a line resistance of 500 kΩ, the bimodal operation and memory of the dc pixel at $V = 225$ V is evident in the figure. If an applied voltage of 225 V is approached from the low-voltage direction, the pixel remains *off*. If, on the other hand, a large voltage is applied and subsequently lowered to $V_a = 225$ V, then the pixel will be in an *on* state. Note that the region where the 225 V/500 kΩ load line intersects the negative resistance portion of the *I–V* characteristic is unstable. The pixel discharge will quickly transition to either the stable *on* or stable *off* operating point. As a practical matter, one should note that the negative resistance region of the *I–V* characteristic curve cannot be experimentally measured in a pixel circuit operating with a 500 kΩ series resistance. Instead, as shown in the figure, a much larger series resistor, $R = 5$ MΩ, provides a load line with slope small enough to produce stable operation in the negative resistance regime.

Electrical Properties of Ac Pixels

The physical design of an opposed electrode ac pixel is shown in Figure 33.5b. Electrically, the pixel functions as a breakdown capacitor and is described by the circuit equation:

$$V_a(t) = I(t)R + \frac{1}{C}\int_0^t I(t')\mathrm{d}t' = I(t)R + Q(t)/C \tag{33.7}$$

where V_a is the externally applied voltage, I the circuit current, C the pixel capacitance, and Q the charge collected. For ac pixels the line resistance, R, is minimized in order to minimize power consumption and Equation 33.7 simplifies to

$$V_a(t) = \frac{1}{C}\int_0^t I(t')\mathrm{d}t' = Q(t)/C \tag{33.8}$$

The capacitance for each pixel is the series summation of the capacitance for each dielectric film and for the gas gap:

$$\frac{1}{C} = \frac{1}{C_{PbO}} + \frac{1}{C_{MgO}} + \frac{1}{C_{gas}} \tag{33.9}$$

In each case,

$$C_i = \frac{e_i A}{d_i} \tag{33.10}$$

where i is the material index and the surface area, A, is roughly equal to the square of the conductor wire width. As shown in Figure 33.5b, an ac pixel is typically constructed with a PbO film of thickness d = 25 μm, while the thin-film MgO has thickness d = 50 to 200 nm. The lead oxide has a dielectric constant of roughly $\varepsilon_{PbO} = 15\varepsilon_0$, while that for MgO is $\varepsilon_{MgO} = 6\varepsilon_0$ with exact values dependent upon the film purity and microstructure [45]. Note that the MgO contribution to the total capacitance is negligible and that this material is incorporated into the design because of its excellent secondary electron emission properties. Prior to gas breakdown, the capacitance of the pixel is attributed largely to the gas gap. For 20 μm-thick conductor wires the capacitance of a pixel gas gap prior to breakdown is about 500 pF. The time derivative of Equation 33.8 gives the circuit current:

$$I(t) = C\frac{\mathrm{d}V(t)}{\mathrm{d}t} \tag{33.11}$$

This charge displacement current appears as the initial large amplitude current peak in Figure 33.13, which shows the temporal current response of a 45 × 45 ac pixel array to a single pulse within a 50 kHz square wave applied voltage pulse train. The electrical measurement shown was made using a simple induction loop probe to measure the current and a high impedance voltage probe (1 MΩ, 3 pF) to monitor the applied voltage. The signals were captured using a high-speed (300 MHz) oscilloscope.

If the applied voltage amplitude is below the gas breakdown threshold, only the capacitor charging displacement current, defined by Equation 33.11, is observed as shown in Figure 33.13a. If the voltage for gas breakdown is exceeded, a second current pulse due to the plasma discharge current within the gas gap is observed in the circuit, Figure 33.13b. The plasma pulse is accompanied, of course, by strong photon emission from the gas gap region. The total charge displacement in the discharge pulse as a function of amplitude of the square wave–applied voltage is plotted in Figure 33.14 for a helium–xenon (2%) Penning gas mixture [35]. The hysteresis or inherent memory property of the ac pixel is apparent. As the applied voltage amplitude is increased from zero to 180 V, no measurable current flows across the pixel gas gap. When no surface charge is present, below 180 V the electric field within the gap region is insufficient to drive the electron collisions into the avalanche regime. For any voltage amplitude in excess of 180 V, a gas discharge is initiated and the pixel turns *on*. If a pixel is subjected to a single voltage pulse with amplitude less than 135 V, the pixel turns *off* even if a surface charge is present.

In ac pixels, charge pairs produced during one discharge pulse collect on the surfaces of the dielectric films at the boundaries of the gas gap and are available to assist formation of the next discharge pulse in the sequence. In a fully developed ac pixel discharge, the surface charge accumulation on the dielectric film produces an electric field within the gas gap, which cancels the gap field produced by the externally applied voltage. This is shown in Figure 33.15, which is a composite representation of experimental current measurements and computational model predictions of the surface charge accumulation producing the surface or wall voltage [34,36]. When the polarity of the applied voltage is reversed, the

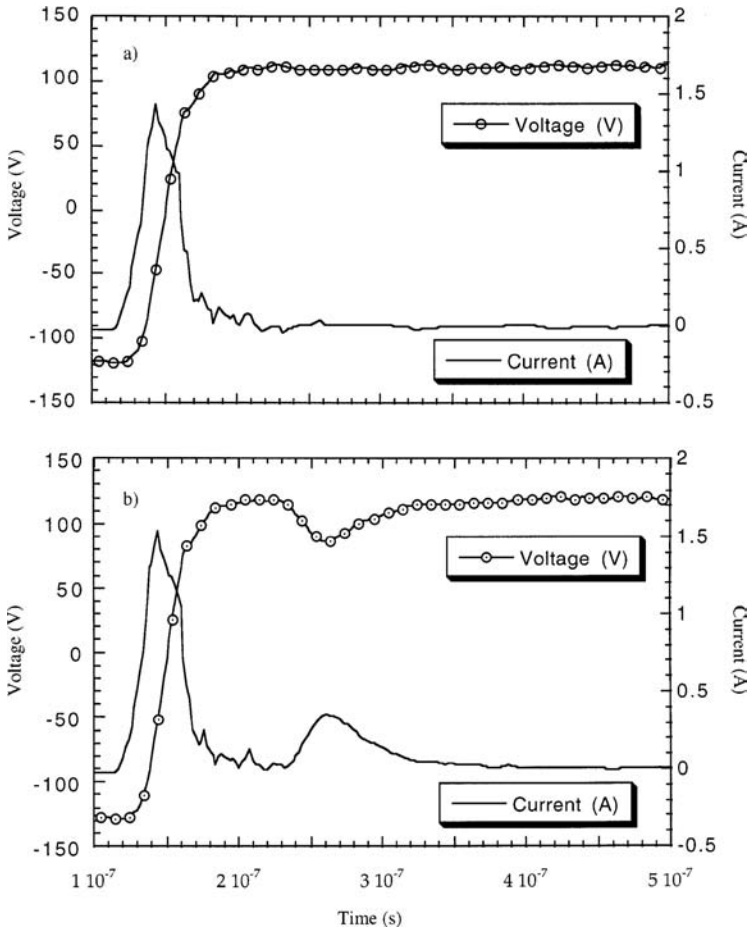

FIGURE 33.13 Voltage and current traces for a 45 × 45 array of ac plasma pixels in the (a) *on* and (b) *off* states. Drive voltage amplitudes were 117 and 127 V, respectively.

potential drop due to the surface charge and that due to the applied voltage suddenly are additive as shown in the figure. The gas gap is momentarily subjected to an intense electric field which results from a potential drop roughly equal to twice the applied voltage. The presence or absence of surface charge results in the bimodal current–voltage behavior shown in Figure 33.14.

Addressing of ac pixels is easily accomplished by taking advantage of the inherent memory of the pixel that results from this bimodal *I–V* behavior. For the pixel electrical properties shown in Figure 33.14, each pixel would be continuously supplied with an ac square wave applied voltage pulse train with an amplitude of 160 V, called the sustain voltage, $V_{sustain}$. If the pixel is initially in an *off* state, it will remain so indefinitely since no surface charge is available to enhance the field produced by the sustain voltage. To turn the pixel *on*, a single high-amplitude voltage pulse, called an address (or write) pulse is delivered across the pixel electrodes. In this example, an address pulse of 200 V initiates a discharge whose charge pairs collect on the internal dielectric surfaces of the pixel. The self-limiting nature of the ac pixel is such that the surface charge concentration produced for a fully developed pixel discharge completely shields the gap region from the externally applied field. When the next sustain polarity reversal occurs, the pixel gas gap experiences a voltage equal to the sum of the sustain voltage (160 V) plus the voltage due to the surface charge produced by the previous pulse, $V_{surface}$ = 200 V in this case. The new gap voltage of 360 V is more than sufficient to initiate a second discharge and to establish a new surface charge whose polarity is opposite that of the preceding pulse. Once again, the surface charge adjusts to produce a

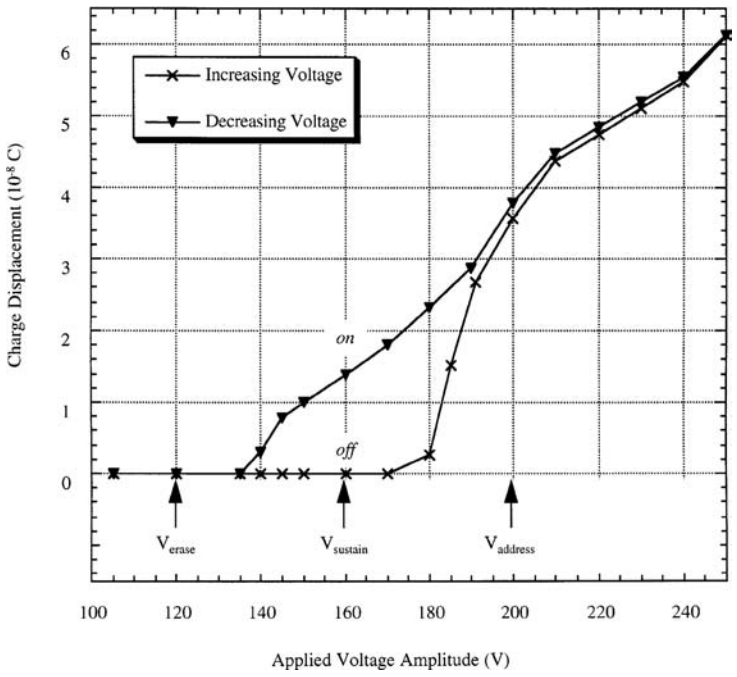

FIGURE 33.14 Discharge charge displacement for operation of a 45 × 45 array of ac-opposed electrode pixels with an He – Xe (2%) gas mixture at 53.3 kPa (400 torr).

voltage exactly canceling the field of the applied voltage. For this pulse, V_{wall} = 160 V, and the next sustain voltage polarity reversal subjects the gap to a potential difference of $V_{gap} = V_{sustain} + V_{address}$ = 160 V + 160 V = 320 V, which is again sufficient to initiate a new discharge pulse. Consequently, the pixel remains in the *on* state until action is taken to eliminate or diminish the surface charge buildup accompanying each discharge. This is accomplished by application of a single low-voltage pulse called an erase pulse with amplitude V_{erase} = 120 V for the example shown in Figures 33.14 and 33.15. Application of the erase pulse produces a potential drop across the gas gap of $V_{gap} = V_{applied} + V_{surface} = V_{erase} + V_{surface}$ = 120 V + 160 V = 280 V. The erase pulse produces a discharge of lower intensity which is insufficient to reestablish a reversed polarity surface charge. Consequently, the erase discharge diminishes the concentration of the surface charge so that no discharge is initiated during the next pulse in the sustain applied voltage train. Ideally, the erase pulse drives the surface charge concentration identically to zero, but this rarely occurs in practice and is not essential for ac pixel operation, as can be seen in Figure 33.15. Very low intensity discharges with negligible photon production drive the pixel to its ideal *off* state within a few ac cycles. Fortunately, these minor deviations from the ideal *off* condition have little effect on subsequent write pulses for frequency-modulated ac operation, and therefore do not affect the timing of pixel addressing and refresh which is covered in the next subsection.

33.4 Display Priming, Addressing, Refresh, and Gray Scale

Pixel priming is necessary to provide the initial source of electrons, or the priming current, required to initiate a discharge avalanche. Metastable atoms or photons can also be used as priming particles since these produce electrons via ionization of the background gas. Pilot cell priming and self-priming are two options used in currently available commercial products. In pilot cell priming, a separate cell which generates electrons is located near the pixel to be addressed. Pilot cells are often located on the periphery of the display outside the viewing area, yet can produce seed electrons throughout the display. In self-priming, an auxiliary discharge created within each pixel provides the priming electron source for the

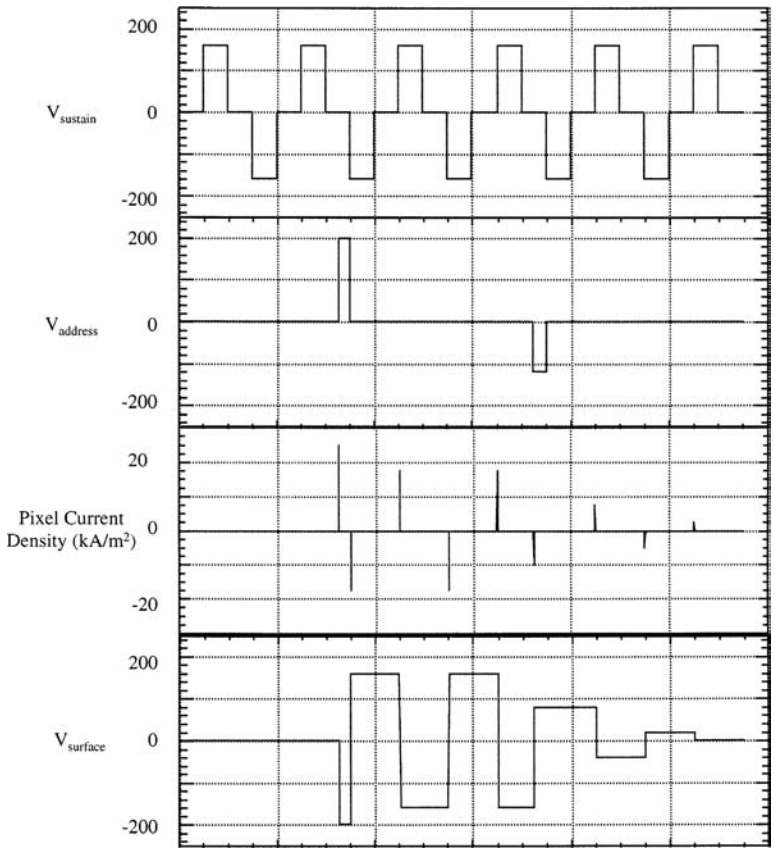

FIGURE 33.15 Sustain and address voltage waveforms for ac-driven plasma pixels. The amplitude of the pixel current density and wall voltage resulting from the surface charge buildup provide a measure of the discharge intensity.

main pixel discharge. These priming discharges are often hidden from view by positioning them behind opaque conductor wires. Introducing a trace amount of radioactive Kr^{85} into the gas mixture provides a passive priming option. The ionizing radiation from Kr^{85} generates priming electrons uniformly throughout the display interior. Because the required Kr concentration is low and because the beta radiation produced cannot penetrate the glass enclosure of the display, the radiation exposure risk to the display user is negligible. However, display manufacture using radioactive seeding involves potential health hazards associated with radioactive material handling. Consequently, this seeding approach, while very effective, is not at present employed in commercial products.

A simplistic scanning scheme for pixel illumination is shown in Figure 33.2, reproduced here from Reference 4. The scan switches on one axis open and close sequentially in a repetitive fashion, while the data switches on the other axis determine if the pixel is fired on a given scan. This simplistic refresh and data update method fails to take advantage of the discharge properties or inherent memory functions available with plasma pixels. High-resolution dynamic displays utilizing this address scheme would not be cost-competitive since display drivers constitute a significant portion of the total cost of plasma displays. Driver circuit costs also increase with required output voltage. Thus, it is desirable to design plasma displays with operating voltages as low as possible and which require the fewest number of driver chips. Designers strive then to maximize the number of pixels driven by a single chip.

For nonmemory dc pixels, one option for reducing the number of external drive switches required is to sweep the firing of priming discharges repetitively across each pixel row, such as in the self-scan circuitry developed by Burroughs [46,47]. More recently, NHK has developed a pulse memory drive scheme for its 102 cm (40 in.) diagonal dc HDTV plasma display, which is being widely used [48]. Sustain

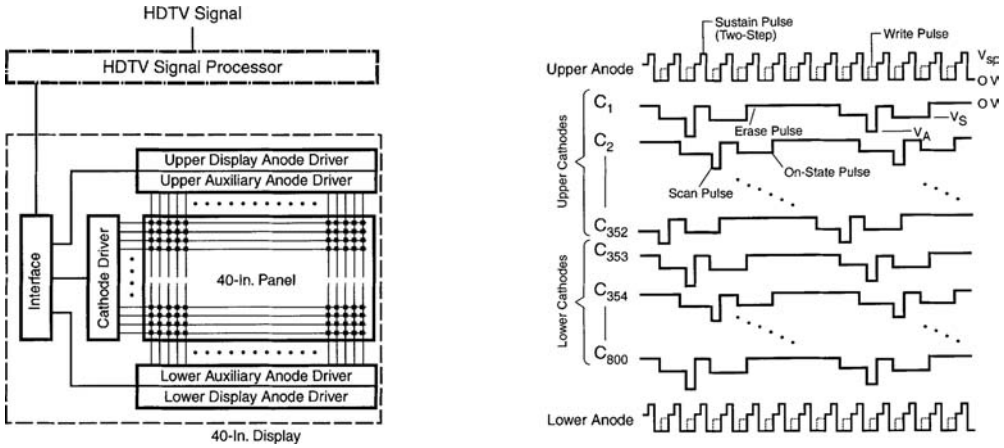

FIGURE 33.16 Pulsed memory operation of the NHK dc plasma display. (a) Block diagram of the driver system and pixel array. (b) Temporal sequences for pulsed memory operation. (From Yamamoto, T. et al., *SID '93 Sympos. Dig.,* 165–168, 1993. With permission.)

operation at high frequency is used to take advantage of residual charge pairs and metastable atoms present in the pixel gas volume as result of the preceding discharge [49]. In this fashion, each pixel is self-seeding, with seed particle populations dependent upon the time elapsed since the termination of the preceding discharge. The high-frequency operation is fast enough to take advantage of the short duration memory characteristic of the dc pixel. As the sustain voltage pulse train is applied to the electrode of a pixel, it will remain in the *on* or *off* state indefinitely until an address or erase pulse is supplied. In the NHK scheme, an auxiliary anode is used to assist in the *address* access operations. Figure 33.16a shows the block diagram of such a system, while Figure 33.16b shows the time sequences for the scheme [48]. Note that the pulses are dc and that *on* state pulses have larger gap voltages than erase pulses. The timing sequence is critical to address a pixel selectively within the matrix. Implementation of this scheme requires (1) display anode drivers, (2) auxiliary anode drivers, (3) cathode drivers, and (4) interfaces to decode the HDTV signals provided to the drivers.

For ac displays with memory, drivers need to provide (1) *address* (or *write*) pulses, (2) *sustain* pulses, and (3) *erase* pulses. A complex refresh scan signal is not required since a continuously supplied sustain signal, coupled with the ac pixels inherent memory, trivially maintains each pixel in either an *on* or *off* state. Pixels respond to address, sustain, and erase pulses as described in the preceding section. Similar to dc pixel dynamic control discussed above, ac pixel addressing requires well-timed application of voltage waveforms to the rows and columns of the display matrix so that the proper voltage appears across the electrodes for the pixel of interest without modifying the state of adjacent pixels. A more-detailed discussion of ac pixel addressing can be found in Reference 4 or 47.

Gray scale is achieved for dc or ac plasma displays either by modulation of the discharge current or by duty cycle modulation with fixed current. Modulating the applied voltage amplitude to vary the discharge current is not widely used because of practical limitations in effectively controlling the nonlinear response of the discharge current. However, duty cycle modulation is a viable technique both for pulse memory-driven dc displays and for ac memory displays. In either case, duty cycle modulation requires complex circuit design for the well-timed delivery of *on* and *off* pulses. Gray scale is achieved by varying the time a pixel is *on* compared with *off* during each refresh cycle. In 50 kHz operation, a sustain half cycle is 10 μs. VUV photon emission occurs usually in less than 1 μs. For color displays the visible light emission persists much longer, with the fastest phosphors having 10% persistence times of about 5 μs. More typical phosphors have 10% persistence times in the 5 to 10 ms range [50]. If the image is updated every 40 ms, corresponding to a refresh rate of 25 images per second, then a 1/8-level brightness is achieved by having the pixel *on* for 5 ms and *off* for 35 ms during that refresh cycle. The time *on* is

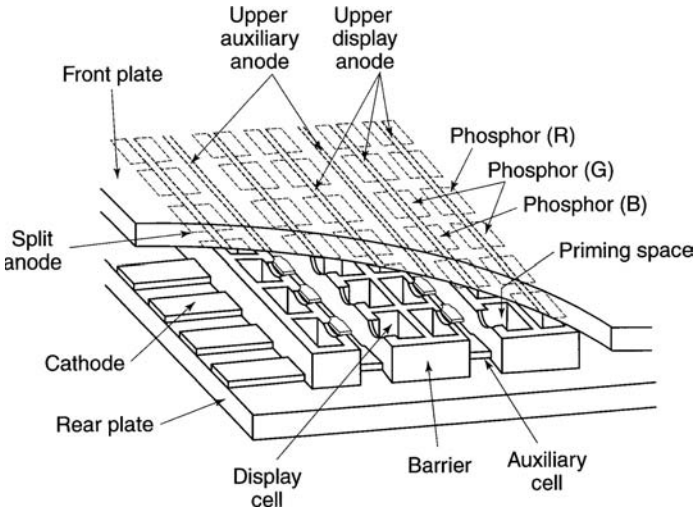

FIGURE 33.17 Structure of the 40 in. color display manufactured by NHK. (From Yamamoto, T. et al., *SID '93 Sympos. Dig.,* 165–168, 1993. With permission.)

interspersed throughout the 40 ms refresh period by appropriate timing circuit design. For example, the NHK 102 cm (40 in.) display has a 2^8 or 256 levels of gray scale per color, providing a total of 16 million (256^3) color scale levels [48].

33.5 Color Plasma Flat Panel Displays

Color Pixel Structures

In color plasma display panels, photoluminescent phosphors provide the primary RGB optical emissions required for full-color image display. In this case, visible emissions from the discharge itself must be suppressed in order to avoid color contamination. A common approach is to utilize xenon as the minority species constituent in the Penning gas mixture of the panel. The structure and phosphor layout of the 102 cm (40 in.) diagonal color dc plasma display available from NHK is shown in Figure 33.17, while that of the Fujitsu 53 cm (21 in.) diagonal ac color display is shown in Figure 33.6. Each uses screen printing and hard mask or abrasive-resistant lithographic processes for conductor wire deposition, barrier structure definition, and phosphor deposition [51]. In the NHK design, the fourth section within the honeycomb color pixel structure houses a redundant green phosphor subpixel to compensate for the lower photoluminance of green phosphors relative to that of either red or blue phosphors. In a similar honeycomb dc color pixel structure, Panasonic instead incorporates a series resistor in this fourth subpixel position [20]. Printing the series resistor for each pixel on the display glass substrate complicates panel manufacturing but simplifies design requirements for the drive electronics. In the Fujitsu, the opposed electrode ac color pixel structure shown in Figure 33.6, barrier or separation rib structures running between and parallel to each conductor wire are fabricated on the rear glass substrate. The barrier rib heights are typically 100 to 150 μm. ac barrier rib structures and dc pixel honeycomb lattice structures are usually composed of the same PbO thick-film dielectric used to cover the conductor wires.

VUV Photon Production and Utilization for Color Plasma Flat Panel Displays

Color plasma display gas mixtures utilizing xenon as the minority species are optimized for production of VUV emissions which are used to excite RGB photoluminescent phosphors. Both neon–xenon and

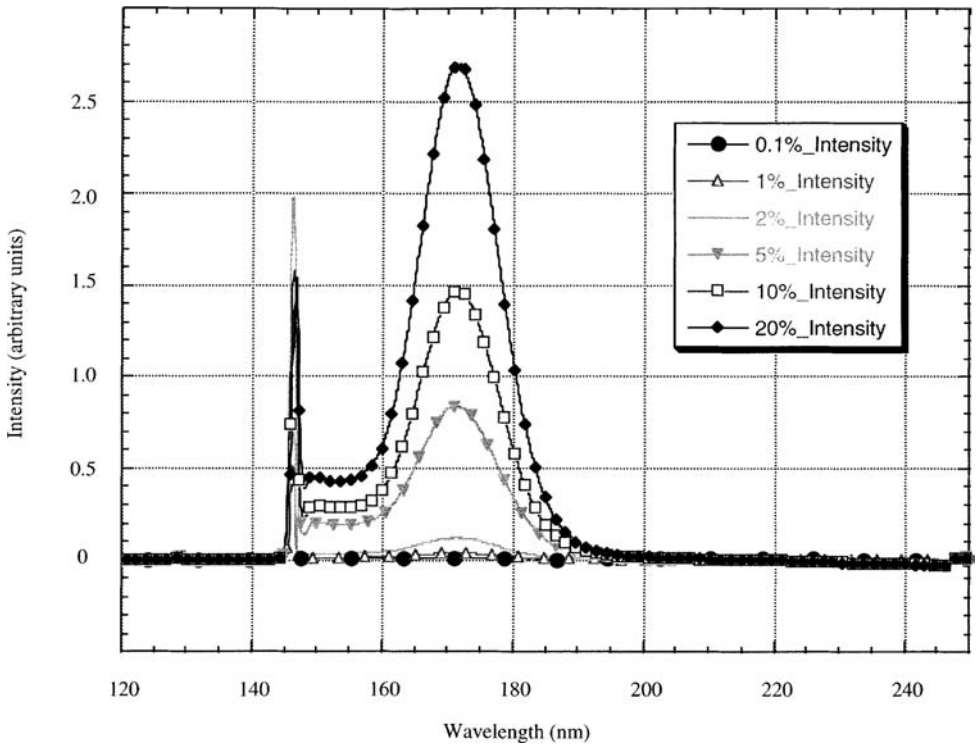

FIGURE 33.18 VUV emission spectra from opposed electrode ac plasma pixel discharges in He/Xe gas mixtures. Each spectrum was collected near the minimum sustain (or first *on*) voltage for that gas mixture, which ranged from 150 V for 0.1% Xe to 350 V for 20% Xe.

helium–xenon combinations are popular. The ionization energy of xenon at 12.3 eV lies below the lowest excited atomic states of either neon or helium, as shown in Figure 33.8. Consequently, electrons accelerated by electric fields within the pixel volume preferentially impart their kinetic energy to the xenon atoms. In addition, the excited states of He or Ne produced readily transfer stored energy to the xenon atoms through ionizing Penning collision processes. Consequently, the red-orange visible emissions typical of Ne discharges are suppressed as Xe concentration is increased. Fujitsu utilizes an Ne–10% Xe working gas in its color display [18], while Photonics Imaging prefers to use an He-based background gas in its panel [23] where suppression of unwanted optical emissions from the discharge can be accomplished at somewhat lower xenon concentrations.

The tendency of xenon to fill its outermost electronic shell results in the formation of the xenon dimer molecule, Xe_2^*, whose energy states are also shown in Figure 33.8 [52,53]. Radiative dissociation of the dimer produces photons with wavelengths near 173 and 150 nm. Figure 33.18 shows how the dimer emissions dominate the VUV spectra from He–Xe gas pixel discharges as the fraction of Xe is increased. Since VUV photons are completely absorbed by glass, the spectra shown in the figure were measured by mounting opposed electrode pixels inside of a vacuum chamber filled with the gas mix of interest. The boundaries of the panel glass were not sealed which then allowed on-edge viewing of the pixel discharges with a McPherson 0.2 m monochromator operating in conjunction with a Princeton Instrument CCD optical multichannel analyzer [34]. The background gas mix was varied to obtain the various Xe concentrations in He shown while maintaining a total gas pressure of 53.3 kPa (400 torr). At low Xe concentrations, photons from the atomic Xe $1s^4$ and $1s^5$ states dominate the emission spectra producing lines at 147 nm and, with much less intensity, at 129 nm. The Tachibana laser-induced spectroscopic measurements show the spatial and temporal evolution of the $1s^4$ Xe atomic state in He/Xe plasma display discharges [54]. Both of these atomic lines experience significant resonant absorption and reemission.

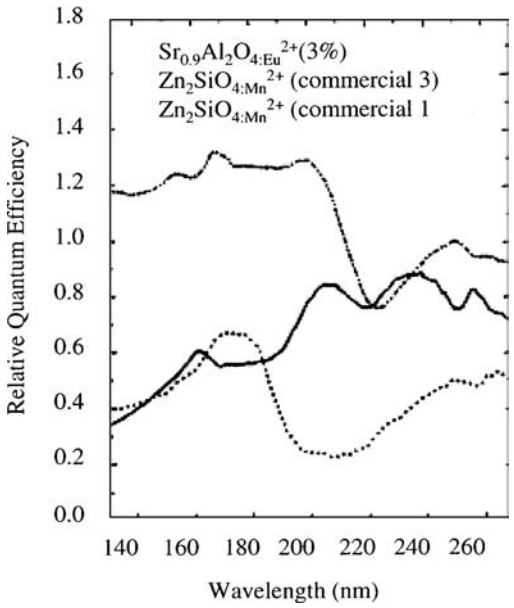

FIGURE 33.19 Relative quantum efficiencies of a Tb-activated lanthanum phosphate compared to that of yttrium and gadolinium phosphate prepared by Sarnoff Research Center. (From Yocum, N. et al., *J. SID*, 4/3, 169–172, 1996. With permission.)

Thus, the measured line intensities are strong functions of photon path length traveled and of Xe partial pressure in the background gas [55]. For the emission spectra shown in Figure 33.18, the lithium fluoride (LiF) entrance window to the evacuated spectrometer chamber was positioned between 100 and 150 nm from the nearest pixel discharges, which is roughly the location of the phosphors relative to the discharge in an opposed electrode ac color display panel; for an example, see Figure 33.5.

Recall that the optimal charge pair production per volt applied in Penning gas discharges occurs at minority species concentrations as low as 0.1%; see Figure 33.9. However, color plasma pixels must optimize usable photon production per watt while maintaining stringent color purity requirements. Consequently, color plasma pixels typically operate with xenon concentrations ranging between 2 and 10%. Figure 33.18 shows that increased xenon concentration results in significant dimer formation and radiative emission from dimer dissociation. Since the dimer dissociation is a three-body process involving a photon and two xenon atoms, the momentum and energy conservation equations do not demand unique solutions. Consequently, emissions lines produced cover a broad spectral range spanning several tens of nanometers. Increased dimer emission is accompanied by the suppression of xenon atomic emission as energy within the atomic manifolds continues to flow toward the lowest available atomic levels; see Figure 33.8. Note, too, that the dimer emission lines are not subject to resonant absorption. Therefore, the measured intensities shown reflect dimer emission from all pixel rows within the line of site of the spectrometer (four for the data of Figure 33.18). In contrast, due to the strong resonance absorption of the atomic lines, more than 90% of the measured intensity of the 147 nm line is produced in the pixel row adjacent to the spectrometer window [34,55]. Care must be taken to account for these large variations in photon mean free paths when analyzing emission data.

Phosphor Excitation and Emission for Color Plasma Flat Panels

A variety of photoluminous phosphors are commercially available. Efficiencies for conversion of VUV photons to visible emissions has a complex dependence on excitation photon wavelength as can be seen in Figure 33.19, which shows quantum conversion efficiencies relative to a sodium salicylate standard for some of the available green phosphors [50]. Conversion efficiencies for red, blue, and other green

TABLE 33.2 Relative Quantum Efficiencies (QE) and Chromaticity Coordinates for Selected Phosphors [50,57]

Phosphor	Rel. QE[a] (174 nm)	Rel. QE[a] (170 nm)	Lifetime (10%) ms	*x*	*y*
NTSC green				0.21	0.71
$(La_{0.87}Tb_{0.13})PO_4$	1.1	1.4	13	0.34	0.57
$(La_{0.6}Ce_{0.27}\ Tb_{0.13})PO_4$	1.1	1.5	12	0.33	0.59
$(Y_{0.85}Ce_{0.1}Tb_{0.05})PO_4$	1.1	1.1	—	—	—
$(Y_{0.6}Ce_{0.27}Tb_{0.13})PO_4$	1.35	1.35	—	—	—
$(Gd_{0.87}Ce_{0.1}Tb_{0.03})PO_4$	1.0	1.1	10	0.34	0.58
$(Gd_{0.6}Ce_{0.27}Tb_{0.13})PO_4$	1.35	1.45	—	—	—
$(Ce,Tb)MgAl_{11}O_{19}$	0.9	1.4	—	—	—
$Sr_{0.9}Al_2O_4:Eu^{2+}$ (3%)	0.4	0.7	0.01	0.26	0.59
Zn_2SiO_4:Mn	1.2	1.3	12.5	0.21	0.72
Zn_2SiO_4:Mn	1.1	1.5	9.8	—	—
Zn_2SiO_4:Mn	0.45	0.55	5.4	—	—
Zn_2SiO_4:Mn	1.0	1.1	5	—	—
Zn_3SiO_4:Mn	1.0			0.21	0.72
$BaAl_{12}O_{19}$:Mn	1.1			0.16	0.74
$BaMgAl_{14}O_{23}$:Mn	0.92			0.15	0.73
$SrAl_{12}O_{19}$:Mn	0.62			0.16	0.75
$ZnAl_{12}O_{19}$:Mn	0.54			0.17	0.74
$CaAl_{12}O_{19}$:Mn	0.34			0.15	0.75
YBO_3:Tb	1.1			0.33	0.61
$LuBO_8$:Tb	1.1			0.33	0.61
$GdBO_3$:Tb	0.53			0.33	0.61
$ScBO_8$:Tb	0.36			0.35	0.60
$Sr_4\ Si_8\ O_8\ Cl_4$:Eu	1.3			0.14	0.33
NTSC red				0.67	0.33
Y_2O_3:Eu	0.67			0.65	0.34
Y_2Si_{O5}:Eu	0.62			0.66	0.34
$Y_3A_{l5}O_{12}$:Eu	0.47			0.63	0.37
$Zn_8(PO_4)_2$:Mn	0.34			0.67	0.33
YBO_3:Eu	1.0			0.65	0.35
$(Y,Gd)BO_8$:Eu	1.2			0.65	0.35
$GbBO_3$:Eu	0.94			0.64	0.36
$ScBO_3$:Eu	0.94			0.61	0.39
$LuBO_8$:Eu	0.74			0.63	0.37
NTSC blue				0.14	0.08
$CaWO_4$:Pb	0.74			0.17	0.17
Y_2SiO_5:Ce	1.1			0.16	0.09
$BaMgAl_{14}O_{23}$:Mn	1.6			0.14	0.09

[a] QEs above double rule are relative to sodium salicylate, those below relative to Zn_2SiO_4:Mn.

phosphors can be found in References 56 and 57. Table 33.2 provides the compositions of some selected commercially available phosphors and lists their relative quantum efficiencies for the principal emission lines of xenon discharges. Note that quantum efficiencies listed are relative values and that phosphors that convert 8.4 eV photons to visible photons near 2.3 eV have absolute efficiencies of only 27%. In principle, it is possible to produce two or more visible photons from a single high energy photon, but to date no such phosphors have been developed [58]. Table 33.2 also lists the chromaticity diagram coordinates which provide a measure of the color purity of the visible RGB emission spectra produced. The chromaticity diagram can be found in many references including Reference 59. Another consideration in the plasma display phosphor selection is persistence. Most of the phosphors listed in Table 33.2 require 5 to 13 ms for the emission intensity to decay to 10% of maximum value. For ac pixel operation at

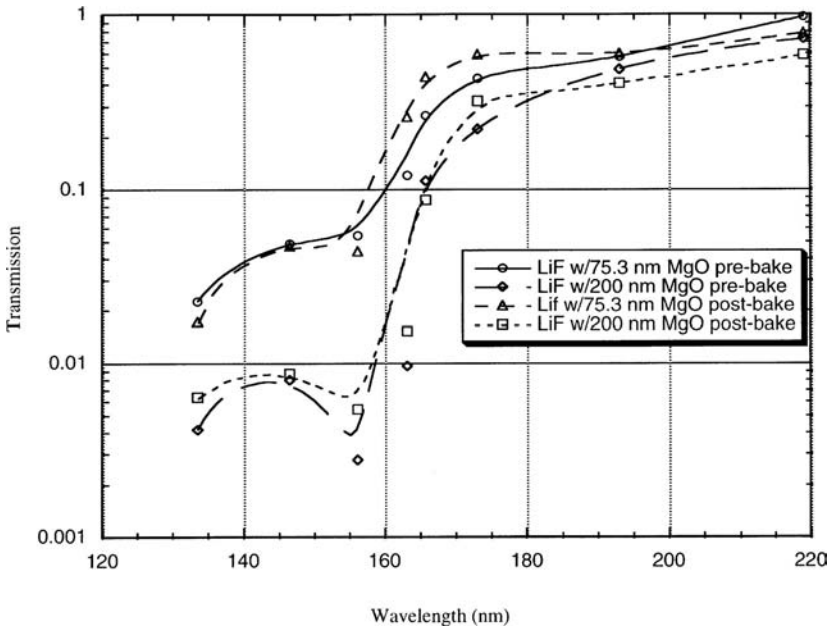

FIGURE 33.20 Photon transmission through MgO films before and after bake-out to remove water vapor.

50 kHz, each sustain voltage half cycle lasts only 10 μs while the discharge produces VUV emissions for only a small fraction of that time. Efforts are continuing for development of phosphors with faster response times. For example, Eu_{2+} green phosphors with 10% decay times of only 5 to 10 μs and with good quantum efficiencies near 173 nm have been developed [50].

Color Plasma Display Lifetime Considerations

Phosphors for plasma flat panel displays must be tolerant of the harsh environment produced by the pixel discharge. Photoluminous phosphor degradation mechanisms are at present not well understood. Contamination of the discharge by phosphor materials is a serious concern. Discharge modeling indicates that damage results principally from the accumulated fluence of photon and metastable bombardment, although fringe electric fields and prolonged surface charge accumulations could also result in ion bombardment [37]. Most ac plasma displays take advantage of MgO for enhancement of the discharge intensity by coating dielectric surfaces above the electrodes with an additional thin film of MgO. For ease of fabrication, the MgO is most often deposited using electron beam evaporation as one of the final manufacturing steps before glass seal and gas fill. If no mask is used, the MgO can also cover the phosphors. While providing the phosphors with a protective coating, the MgO film also attenuates the intensity of the VUV photon flux available to excite the phosphors. Figure 33.20 shows VUV photon transmission as a function of wavelength through MgO films [34,60]. The measurements show that the primary atomic Xe emission lines at 129 and 147 nm are nearly 95% attenuated by an MgO film only 75 nm thick. In contrast, the dimer emission lines centered near 173 nm are much less attenuated with transmission factors of 30 to 50%, respectively, for MgO films of 200 and 75 nm. Consequently, ac plasma display designers must often achieve a balance among discharge enhancement due to MgO secondary electron emission, discharge degradation due to MgO photon absorption, and fabrication complexity associated with MgO deposition, which impacts the final cost of the display. Additionally, the designer must consider the aging or brightness degradation with time of the display, which is influenced in part by the rate of MgO sputter erosion discussed briefly below.

TABLE 33.3 Equipment for Noncontact Profiling and Chemical Characterization of Thin Films

	CyberOptics Point Range Sensor	Zygo NewView 200	Leitz FTM400
Physical principle	Laser triangulation	Scanning white light interferometry	Laser interferometry
Maximum thickness/step height	150 μm (high resolution head)	100 μm (standard) (to 5 mm with z-drive)	70 μm
Vertical resolution	0.38 μm	100 pm	150 pm or 0.5%
Spatial resolution	>0.5 μm	0.22 μm	0.5 μm
Spot diameter/FOV	5.1 μm	140 × 110 μm	20 μm
Scan rate	10 points/s	2 or 4 μm/s	75 mm/s max.
Maximum sample size	Based on Table	10 cm × 15 cm	47 cm × 37 cm
Maximum sample weight	Based on Table	4.5 kg	4.5 kg (including holder)
Elemental detection	N.A.	N.A.	N.A.

33.6 Inspection and Metrology

Plasma display panel manufacturing uses some process steps typically found in semiconductor device manufacturing. Although the feature sizes are much larger than those required in semiconductor manufacturing, the dimensions over which feature integrity must be assured are also much larger. Confirmation that a display manufacturing process is under control or rapid quantitative characterization of the deviation from acceptable process limits is essential to producing high-quality displays with high yield. Information on a variety of length scales is required. Blanket deposition of materials onto substrates should be uniform; large deviations in thickness of the deposited material from one point on the substrate to a widely separated point should be avoided. Similarly, roughness of the deposited layers must be kept within defined limits. Finally, chemical compositions of deposited layers and their spatial homogeneity need to be measured and controlled.

The three commercial profile measuring devices, the CyberOptics, Zygo, and Leitz units, are based on laser or white light triangulation or interferometry; see Table 33.3 [61-63]. These machines are well suited for determining the profile of metallization after patterning. They do not appear to be useful for measuring the thickness of opaque layers and cannot, for example, measure the thickness of the blanket metallization before patterning. The CyberOptics unit is in wide use in the electronic packaging industry because of the low noise in its signal. Improvements in vertical resolution would increase its value for display manufacturing process control. The Zygo instrument has better vertical resolution, but has no real scanning capability. The Leitz unit is designed specifically for metrology of unfinished liquid crystal display components, and is presumably optimized for that application. Both the CyberOptics and Zygo units have a variety of heads with differing resolutions and fields of view. However, the vertical distance over which the interference can take place in the Zygo unit is very limited, so it may not be suitable for measuring features with large vertical dimensions.

Depending on system requirements, a useful laser metrology system can be purchased for as little as $20,000. Full-featured systems can easily cost $100,000. The bulk of the cost is, however, in the precision transport tables used for moving samples in a precisely controlled manner beneath stationary measurement heads. Since precision transport tables meeting the needs of the metrology equipment may already be part of the display production process or would require only minor upgrades to be brought in line with requirements, the cost to bring the metrology capability online may be much smaller than the figures mentioned above. Since laser head costs are low, it may also be desirable to use multiple fixed heads to speed up inspection and metrology.

Listed in Table 33.4 are the characteristics of two advanced measurement techniques for noncontact profiling and chemical analysis. To the authors' knowledge, systems of this type are not yet commercially available. They are being utilized, however, by researchers at Sandia National Laboratories and show

TABLE 33.4 Advanced Techniques for Noncontact Profiling/Chemical Characterization of Thin Films

Physical Principle	β-Backscatter	X-Ray Microfluorescence
Maximum thickness/step height	A few mm	50 μm
Vertical resolution	About 0.1 nm	0.1 μm
Spatial resolution	Depends on pinhole size	50 μm–2 mm
Spot diameter/FOV	Depends on pinhole size	100 μm
Scan rate	<1 min/measurement	1 spot/min
Maximum sample size	No restriction	24 cm × 21.5 cm
Maximum sample weight	No restriction	4.5 kg
Elemental detection	N.A.	<10–300 ppm

promise for commercial usage. In beta backscattering measurements, the energy spectra of the backscattered beta particles provides an accurate measure of the elemental composition of a surface. This technique has been used to measure the thin-film thickness of trace-deposited metals on large-area surfaces (several square meters) in tokamaks [64]. With a depth resolution of about 100 pm, beta backscatter could serve as the physical basis for a high-sensitivity surface-profiling device. X-ray fluorescence measurements, routinely performed in air, can give information on film thickness and composition, and performance parameters for this technique are also listed in Table 33.4. Vacuum must be used when studying light elements like carbon, a potential undesired product of phosphor binder burnout, because the x rays produced are "soft". Although x-ray fluorescence equipment may have good lateral resolution, a larger spot size may prove useful when more averaged information such as film thickness is needed. Finally, eddy current measurements may provide a fast and reliable method for determining the thickness of the opaque, blanket metallization before patterning. This technique should be capable of providing 10% thickness measurement accuracy for conductor layers as thin as 1 μm.

Many of the devices for quantitative characterization of the thickness and chemistry of the deposited layers suffer from the fact that they have a rather limited field of view. Characterization techniques are needed that will allow rapid identification of visual defects in the blanket-deposited layers and in the patterned layers produced from them. Visual inspection equipment is available for defect identification in liquid crystal displays. Manufacturers include Minato Electronics, Advantest, ADS, Photon Dynamics, and Teradyne. All use CCD devices and special algorithms for the identification of line and area defects. The defects found during high-volume plasma display manufacturing may be sufficiently similar in appearance to those found in liquid crystal display manufacturing that this equipment will prove useful with appropriate adjustments. These devices, however, are expensive.

Although researchers and equipment manufacturers believe that the equipment and techniques described above will be suitable for online process control during plasma display manufacturing, all agree that more development is required. Real parts will need to be characterized extensively on specific commercial equipment in production environments before conclusions can be drawn about the suitability of the equipment and techniques for the intended application. This is particularly true for more difficult measurements, like that of the thickness of dielectric above conductor lines. It is clear that there is no single instrument that will meet all film and feature dimensional measurement requirements and those for chemical characterization. A number of instruments will be needed to measure confidently the parameters needed for inspection, and characterize and control the manufacturing processes for plasma displays.

References

1. D.L. Bitzer and H.G. Slottow, The plasma display panel — a digitally addressable display with inherent memory, *1966 Fall Joint Computer Conf.,* Washington, D.C., *AFIPS Conf. Proc.,* 29, 541, 1966.
2. H.G. Slottow, Plasma displays, *IEEE Trans. Electron. Devices*, 23, 760–772, 1976.

3. T.N. Criscimagna and P. Pleshko, Ac plasma display. chap. 3, in *Topics in Applied Physics,* Vol. 40, *Display Devices,* Springer-Verlag, Berlin, 91–150, 1980.
4. L.F. Weber, Plasma displays, chap. 10, in *Flat Panel Displays and CRTs*, L.E. Tannas, Jr., Ed., Van Nostrand Reinhold, New York, 1985.
5. J. Nolan, Gas discharge display panel, *1969 International Electron Devices Meeting,* Washington, D.C., 1969.
6. H.J. Hoehn and R.A. Martel, A 60 line per inch plasma display panel, *IEEE Trans. Electron Devices*, 18, 659–663, 1971.
7. O. Sahni and W.P. Jones, Spatial distribution of wall charge density in ac plasma display panels, *IEEE Trans. Electron Devices*, 25, 223–226, 1979.
8. O. Sahni and C. Lanza, Origin of the bistable voltage margin in the ac plasma display panel, *IEEE Trans. Electron. Devices*, 24, 853–859, 1977.
9. C. Lanza and O. Sahni, Numerical calculation of the characteristics of an isolated ac gas discharge display panel cell, *IBM J. Res. Dev.*, 22, 641–646, 1978.
10. O. Sahni and M.O. Aboelfotoh, The pressure dependence of the bistable voltage margin of an ac plasma panel cell, *Proc. SID*, 22, 212–218, 1981.
11. O. Sahni and C. Lanza, Importance of the secondary electron emission coefficient on E/Po for Paschen breakdown curves in ac plasma panels, *J. Appl. Phys*., 47, 1337, 1976.
12. O. Sahni and C. Lanza, Influence of the secondary electron emission coefficient of argon on Paschen breakdown curves in ac plasma panels for neon + 0.1% argon mixture, *J. Appl. Phys*., 47, 5107, 1976.
13. C. Lanza, Analysis of an ac gas display panel, *IBM J. Res. Dev.,* 18, 232–243, 1974.
14. O. Sahni, C. Lanza, and W.E. Howard, One-dimensional numerical simulation of ac discharges in a high-pressure mixture of Ne + 0.1% Ar confined to a narrow gap between insulated metal electrodes, *J. Appl. Phys*., 49, 2365, 1978.
15. O. Sahni and C. Lanza, Failure of Paschen's scaling law for Ne –0.1% Ar mixtures at high pressures, *J. Appl. Phys*., 52, 196, 1981.
16. H. Wakabayshi, Display market projections report from Namora Research Institute, paper presented at *Imaging 2001: The U.S. Display Consortium Business Conference*, January 28, 1997, San Jose, CA.
17. K. Werner, Plasma hits the ground running, *Inf. Display*, 12(12), 30–34, 1996.
18. *Nikkei Materials & Technology*, [135], November, 1993, pp. 22–23.
19. H. Murakami and R. Toyonaga, A pulse discharge panel display for producing a color TV picture with high luminance and luminous efficiency, *IEEE Trans. Electron Devices*, 29, 988, 1982.
20. M. Ushirozawa, Y. Motoyama, T. Sakai, K. Wani, and K. Takahashi, Color DC-PDP with an improved resistor design in each cell, paper 33.2, pp. 719–722, *SID '94 Symp. Dig*., 1994.
21. S. Mikoshiba, Color plasma displays: where are we now?, *Inf. Display*, 10(10), 21, 1994.
22. Y. Takano et al., A 40-in, DC-PDP with new pulse memory drive scheme, *SID '97 Dig*., 1997.
23. P.S. Friedman, Are plasma display panels a low-cost technology?, *Inf. Display*, 11(10), 22–25, 1995.
24. *Inf. Display*, 10(7 & 8), 28, 1994.
25. A. von Engle, *Ionized Gases,* AIP Press, New York, 1994.
26. S. Brown, *Basic Data of Plasma Physics — The Fundamental Data on Electrical Discharges in Gas*, American Institute of Physics Press, New York, 1993.
27. F.F. Chen, *Introduction to Plasma Physics*, Plenum Press, New York, 1977.
28. D. Miller, J. Ogle, R. Cola, B. Caras, and T. Maloney, An improved performance self-scan I panel design, *Proc. SID*, 22, 159–163, 1981.
29. M.H. Miller and R.A. Roig, Transition probabilities of XeI and XeII, *Phys. Rev. A*, 8, 480, July 1973.
30. *Atomic Data and Nuclear Data Tables*, Vol. 21, No. 6, Academic Press, New York, 1978.
31. R.S. Van Dyck, C.E. Johnson, and H.A. Shugart, Lifetime lower limits for the $^3P_0$ and $^3P_2$ metastable states of neon, argon and krypton, *Phys. Rev. A*, 5, 991–993, 1972.
32. A.A. Kruithof and F.M. Penning, The Townsend ionization coefficient and some elementary processes in neon with small admixtures of argon, *Physica,* 4(6), 450, 1937.

33. F.L. Jones and W.R. Galloway, The sparking potential of mercury vapor, *Proc. Phys. Soc. Lond.*, 50, 207–212, 1938.
34. R.T. McGrath, R. Veerasingam, J.A. Hunter, P.D. Rockett, and R.B. Campbell, Measurements and simulations of VUV emissions from plasma flat panel display pixel microdischarges, *IEEE Trans. on Plasma Sci.,* 26(5), 1998.
35. P. Hines, Spectroscopic and electrical measurements on opposed electrode ac plasma display pixels, Honors engineering senior thesis, The Pennsylvania State University, University Park, 1997.
36. R. Veerasingam, R.B. Campbell, and R.T. McGrath, One-dimensional single and multipulse simulations of the ON/OFF voltages and bistable margin for He, Xe, and He/Xe filled plasma display pixels, *IEEE Trans. Plasma Sci.*, 24(6), 1399–1410, 1996.
37. R. Veerasingam, R.B. Campbell, and R.T. McGrath, Two-dimensional simulations of plasma flow and charge spreading in ac plasma displays, *IEEE Trans. Plasma Sci.*, 24, 1411–1421, 1996.
38. M. Scott, Los Alamos National Laboratory, Private communication, 1997.
39. H. Uchike, K. Miura, N. Nakayama, T. Shinoda, and Y. Fukushima, Secondary electron emission characteristics of dielectric materials in ac-operated plasma display panels, *IEEE Trans. Electron. Devices*, 23, 1211–1217, 1976.
40. N.J. Chou and O. Sahni, Comments on "Secondary Emission Characteristics of Dielectric Materials in ac Operated Plasma Display Panels," *IEEE Trans. Electron. Devices*, 25, 60–62, 1978.
41. T. Shinoda, H. Uchike, and S. Andoh, Low-voltage operated ac plasma-display panels, *IEEE Trans. Electron. Devices*, 26, 1163–1167, 1979.
42. M. Aboelfotoh and J.A. Lorenzen, Influence of secondary-electron emission from MgO surfaces on voltage-breakdown curves in Penning mixtures for insulated-electrode discharges, *J. Appl. Phys.*, 48, 4754–4759, 1977.
43. T. Nenadovic, B. Perraillon, Z. Bogdanov, Z. Djordjevic, and M. Milic, Sputtering and surface topography of oxides, *Nucl. Instrum. Methods Phys. Res.,* B48, 538–543, 1990.
44. Schone, D. Walsh, R.T. McGrath and J.H. Burkhart, Microbeam Rutherford backscattering measurements of flat panel display thin film erosion, *Nuclear Instru. Methods Phys. Rev.-B,* 130(1–4), 543–550, 1998.
45. *CRC Handbook of Chemistry and Physics, 48th ed.*, R.C. Weast and S. M. Selby, Eds., The Chemical Rubber Co., Cleveland, OH, 1967.
46. S. Matsumoto, *Electronic Displays Devices*, John Wiley & Sons, New York, 1990.
47. G.E. Holz, The primed gas discharge cell — a cost and capability improvement for gas discharge matrix displays, *Proc. SID,* 13(2), 1972.
48. T. Yamamoto, T. Kuriyama, M. Seki, T. Katoh, H. Murakami, K. Shimada, and H. Ishiga, A 40 in. diagonal HDTV plasma display, *SID' 93 Symp. Dig.,* 165–168, 1993.
49. J. Deschamps and H. Doyeus, Plasma displays, *Phys. World*, June 1977.
50. N. Yocum, R.S. Meltzer, K.W. Jang, and M. Grimm, New green phosphors for plasma displays, *J. SID*, 4/3, 169–172, 1996.
51. H. Fujii, H. Tanabe, H. Ishiga, M. Harayama, and M. Oka, A sandblasting process for fabrication of color PDP phosphor screens, paper 37.5, 728–731, *SID '92 Symp. Dig.,* 1992.
52. M.C. Castex, Experimental determination of the lowest excited Xe_2 molecular states from VUV absorption spectra, *J. Chem. Phys.,* 74, 759–771, 1981.
53. M.R. Flannery, K.J. McCann, and N.W. Winter, Cross sections for electron impact ionization of metastable rare gas excimers (He_2*, Kr_2*, Xe_2*), *J. Phys. B Mol. Phys.,* 14, 3789–3796, 1981.
54. K. Tachibana, Spatio-temperal measurement of excited Xe($1s_4$) atoms in a discharge cell of a plasma display panel by laser induced spectroscopic microscopy, *Appl. Phys*. Lett., 65, 935–937, 1994.
55. T. Holstein, Imprisonment of resonance radiation in gases, *Phys. Rev.*, 72, 1212, 1947.
56. De Husk and S.E. Schnatterly, Quantum efficiency and linearity of 16 phosphors in the soft x-ray regime, *J. Opt. Soc. Am. B*, 9, 660–663, 1992.
57. J. Koike, T. Kojima, and R. Toyonaga, New tricolor phosphors for gas discharge display, *J. Electrochem. Soc. Solid-State Sci. Tech*., 1008, June 1979.

58. P.N. Yocum, Future requirements of display phosphors from an historical perspective, *J. SID*, 4/3, 149, 1996.
59. L.E. Tannas, Jr., Ed., *Flat Panel Displays and CRTs*, Van Hostrand Reinhold, New York, 1985.
60. S.G. McLean and W.W. Duley, VUV absorption in thin MgO films, *J. Phys. Chem. Solids*, 45, 223, 1984.
61. R. Kuntz, CyberOptics, Private communication, 1-800-746-6315.
62. Zygo, Private communication, 1-860-347-8506, www.zygo.com.
63. A. Machura, Leica, Private communication, 49 (0) 6441 29-2316, Andreas.Machura@lmw.leica.com.
64. B.E. Mills, D.A. Buchenauer, A.E. Pontau, and M. Ulrickson, Characterization of deposition and erosion on the TFTR bumper limiter and wall, *J. Nucl. Mater.*, 162–164, 343–349, 1989.